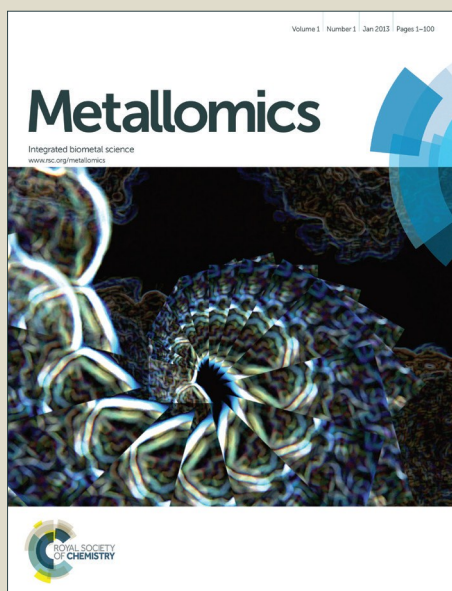


Metallomics

Accepted Manuscript



This is an *Accepted Manuscript*, which has been through the Royal Society of Chemistry peer review process and has been accepted for publication.

Accepted Manuscripts are published online shortly after acceptance, before technical editing, formatting and proof reading. Using this free service, authors can make their results available to the community, in citable form, before we publish the edited article. We will replace this *Accepted Manuscript* with the edited and formatted *Advance Article* as soon as it is available.

You can find more information about *Accepted Manuscripts* in the [Information for Authors](#).

Please note that technical editing may introduce minor changes to the text and/or graphics, which may alter content. The journal's standard [Terms & Conditions](#) and the [Ethical guidelines](#) still apply. In no event shall the Royal Society of Chemistry be held responsible for any errors or omissions in this *Accepted Manuscript* or any consequences arising from the use of any information it contains.

A multimodal imaging workflow to visualize metal mixtures in the human placenta and explore colocalization with biological response markers

Megan M. Niedzwiecki^{1*a}, Christine Austin^{1,2}, Romain Remark³, Miriam Merad³, Sacha Gnjatic³, Guadalupe Estrada-Gutierrez⁴, Aurora Espejel-Nuñez⁵, Hector Borboa-Olivares⁶, Mario Guzman-Huerta⁶, Rosalind J. Wright⁷, Robert O. Wright¹ and Manish Arora^{1*}

¹ Exposure Biology, Senator Frank R. Lautenberg Environmental Health Sciences Laboratory, Department of Preventive Medicine, Icahn School of Medicine at Mount Sinai, New York City, New York, USA

² Faculty of Dentistry, The University of Sydney, Sydney, New South Wales 2006, Australia

³ Division of Hematology/Oncology and Immunology, The Tisch Cancer Institute, Icahn School of Medicine at Mount Sinai, New York City, New York, USA

⁴ Biomedical Research Branch, Instituto Nacional de Perinatología, Mexico City, Mexico

⁵ Department of Immunobiochemistry, Instituto Nacional de Perinatología, Mexico City, Mexico

⁶ Maternal Fetal Research Unit, Instituto Nacional de Perinatología, Mexico City, Mexico

⁷ Mindich Child Health & Development Institute, Icahn School of Medicine at Mount Sinai, New York, New York, USA

1
2
3 *Correspondence to: Manish Arora, Icahn School of Medicine at Mount Sinai,
4
5 Department of Preventive Medicine, One Gustave L. Levy Place, Box 1057, New
6
7 York, NY 10029, USA, manish.arora@mssm.edu; Megan M. Niedzwiecki, Rollins
8
9 School of Public Health, Emory University, 1518 Clifton Road NE, Claudia Nance
10
11 Rollins Building, 5th Floor, Atlanta, GA 30322, USA, mniedz@emory.edu.
12
13

14
15
16 a. Present address: Rollins School of Public Health, Emory University, 1518 Clifton
17
18 Road NE, Claudia Nance Rollins Building, 5th Floor, Atlanta, GA 30322.
19
20

21
22
23 Running title: Metal mixtures and biologic response markers in the placenta
24
25

26
27 Competing Financial Interests: The authors declare no competing financial
28
29 interests.
30
31
32
33
34
35
36
37
38
39
40
41
42
43
44
45
46
47
48
49
50
51
52
53
54
55
56
57
58
59
60

Abstract

Fetal exposure to essential and toxic metals can influence life-long health trajectories. The placenta regulates chemical transmission from maternal circulation to the fetus and itself exhibits a complex response to environmental stressors. The placenta can thus be a useful matrix to monitor metal exposures and stress responses *in utero*, but strategies to explore the biologic effects of metal mixtures in this organ are not well-developed. In this proof-of-concept study, we used laser ablation-inductively coupled plasma-mass spectrometry (LA-ICP-MS) to measure the distributions of multiple metals in placental tissue from a low-birth-weight pregnancy, and we developed an approach to identify the components of metal mixtures that colocalized with biological response markers. Our novel workflow, which includes custom-developed software tools and algorithms for spatial outlier identification and background subtraction in multidimensional elemental image stacks, enables rapid image processing and seamless integration of data from elemental imaging and immunohistochemistry. Using quantitative spatial statistics, we identified distinct patterns of metal accumulation at sites of inflammation. Broadly, our multiplexed approach can be used to explore the mechanisms mediating complex metal exposures and biologic responses within placentae and other tissue types. Our LA-ICP-MS image processing workflow can be accessed through our interactive R Shiny application ‘shinyImaging’, which is available at <https://mniedz.shinyapps.io/shinyImaging/>.

Key words: laser ablation-inductively coupled plasma-mass spectrometry; mass spectrometry imaging; image processing; colocalization; prenatal exposures; metallomics; metal mixtures; biological response; placenta; humans; exposome

Introduction

The adverse health effects of metal exposures—including toxic metal exposures and micronutrient deficiencies and excesses—may be exacerbated or ameliorated when exposure occurs in the context of a mixture.¹ This is of particular importance *in utero*, when critical windows of susceptibility exist for fetal programming events that may trigger negative health outcomes later in life.² In exposure biology, an emerging paradigm is the concept of the pregnancy exposome, which seeks to understand the interactions among all environmental exposures that pass through or are stopped at the placenta,³ as well as simultaneously evaluate the physiological responses to these exposures.^{4,5} An ‘exposomic’ approach has the potential to enable new discoveries about the role of mixed-metal exposures in the fetal origins of disease; however, the successful application of this paradigm is predicated upon the development of novel biomarkers and analytic approaches for assessing multiple exposures simultaneously.

The exposome is a complex concept that involves not only how exposures change over time, but also how a given chemical distributes in the body or even within a tissue. In theory, two people with an identical level of exposure (i.e. dose) may have different biological responses. Inherent in this concept are genetic and epigenetic susceptibility; while genetics and epigenetics no doubt play a role in chemical distribution, many other factors, some of which may be stochastic, also play a role. Thus, how a chemical distributes in a tissue, which is a reflection of where it is binding, may be more informative than only measuring epigenetic or genetic factors that partially drive that distribution difference. Measuring all these factors together is one of the long-term goals of the exposome.

1
2
3 Mass spectrometry imaging (MSI) is a powerful tool for the direct quantitative
4 visualization of the distributions of multiple analytes in tissues.⁶ One common MSI
5 technique, laser ablation-inductively coupled plasma-mass spectrometry (LA-ICP-
6 MS), allows the sensitive, high-resolution spatial mapping of element
7 concentrations.^{7,8} MSI holds great promise for advancing the study of the human
8 exposome, and we propose that multidimensional elemental imaging of placental
9 tissues is a powerful approach to uncover the biologic effects of metal mixtures
10 during pregnancy.⁹ We recognized that the widespread integration of elemental
11 imaging in exposomic research, particularly in large-scale human studies, necessitates
12 a workflow involving the (i) rapid and objective pre-processing of elemental imaging
13 datasets, (ii) integration of data from elemental imaging with other imaging
14 approaches, and (iii) rigorous statistical analysis to quantify the relationships among
15 analytes measured across different imaging modalities.
16
17
18
19
20
21
22
23
24
25
26
27
28
29
30
31

32 With the goal to create a workflow enabling a more nuanced assessment of the
33 biologic impacts of metal mixture exposures in the human placenta, we combined
34 LA-ICP-MS elemental imaging¹⁰ with multiplexed immunohistochemistry (IHC) as a
35 novel approach to measure element and protein distributions within tissues. Here, we
36 present a proof-of-principle example showing how our workflow can be used to
37 assess the spatial associations between metals and markers of inflammation in the
38 placenta.
39
40
41
42
43
44
45
46
47
48
49
50
51
52
53
54
55
56
57
58
59
60

Results

Overview of elemental imaging workflow

The sample collection, preparation and imaging protocol is summarized in **Figure 1**; a video displaying the implementation of our workflow using our interactive software tool shinyImaging (<https://mniedz.shinyapps.io/shinyImaging/>) can be found in **Supplementary Movie 1** and <https://vimeo.com/156307893>. Briefly, tissue was collected from the fetal side of the placenta, fixed in formalin, and embedded in paraffin. Tissue sections (5- μ m thick) were affixed to glass microscope slides and imaged using a LA-ICP-MS system, and signals for the major (or sole) isotopes for elements of interest were collected and assembled into multidimensional grid stacks using our R script, which was written to accompany the R package ‘raster’.¹¹ Our data reduction approach combines all individual .csv data files (or ablation lines) into a single file structured as a stack of matrices, with one element per matrix (**Fig. 1**). Following pre-processing (see **Materials and Methods**), the matrix stack is converted to the RasterStack file format, in which matrices are RasterLayers with identical grid structures (spatial extent and resolution). The element RasterStack can be further analyzed in R or written to a file in numerous single and multiband formats, including but not limited to ascii (.asc), ENVI (.envi), and GeoTiff (.tif).

In quantitative image analysis, the presence of background pixels can lead to biased results and should be removed prior to statistical analyses.¹² Here, we devised a global thresholding algorithm to classify tissue and background pixels uniformly across all layers of a multidimensional element image stack (see **Materials and Methods** for an in-depth description of the algorithm). Briefly, our algorithm calculates the variance in element intensities in the overall image and within the gas-blank region to assess the ability of each element to differentiate between tissue and

1
2
3 background pixels, and a composite ‘mask’ layer is created by calculating the mean
4
5 intensity for each pixel across all elements in the stack, with each element weighted
6
7 on its pixel differentiation ability. Next, kernel density estimation, a non-parametric
8
9 smoothing technique, is used to estimate the probability density function for the mask
10
11 layer. Since the distribution is bimodal (a mixture of two component distributions,
12
13 target and background), the algorithm determines the threshold value by finding the
14
15 value at the first-occurring local minimum in this distribution. Then, the algorithm
16
17 sets all pixels in the mask layer with values below the threshold to null (NA). (If
18
19 necessary, remaining background pixels can be removed using a clump identification
20
21 algorithm that assigns null values to small ‘clumps’ [i.e., patches of connected pixels]
22
23 and/or manually removed using a region-of-interest selection tool.) Finally, an edge
24
25 detection algorithm delineates tissue boundaries to create a final mask layer with
26
27 edge, non-edge, and background pixels assigned values of 1, 0, and NA respectively
28
29
30
31 **(Fig. 1b)**. Masked element stacks are generated by assigning null values to all
32
33 corresponding pixels classified as “NA” in the mask layer, consistently across each
34
35 layer in the stack.
36
37

38
39 Grids then undergo a robust cleaning and smoothing procedure **(Fig. 1c)**. We
40
41 designed an approach for the spatial assessment of local extreme outliers that are
42
43 likely to result from shot noise or other instrumentation-related issues, since clusters
44
45 of high values identified as potential outliers by a global assessment may instead
46
47 represent biologically-relevant areas of metal accumulation. As such, a moving
48
49 window MAD assessment identifies pixels in masked grids with values that exceed
50
51 the local median by a specific magnitude (here, 5 times MAD), while ignoring
52
53 outliers that are located in clusters that are likely to be biologically relevant (see
54
55 **Materials and Methods**). Outliers are replaced using a focal filter that replaces
56
57
58
59
60

1
2
3 values for outliers only. To further reduce noise and remove imaging artefact, grids
4
5 are smoothed with a Gaussian filter, which is performed after outlier removal to
6
7 prevent inadvertent integration of extreme outliers into the final images.
8
9

10 To examine the performance and speed of our workflow, we analyzed
11
12 randomly-selected regions from the fetal and maternal sides from 5 placental samples
13
14 (10 sections in total; 90 ablation lines each). Our masking algorithm was successful
15
16 for all 10 sections and performed excellently despite the presence of shot noise and
17
18 complex tissue architectures (Supplementary Figures 1-10). Using our shinyImaging
19
20 application, we were able to process all 10 samples (raw ablation file upload,
21
22 background correction, masking, outlier removal, smoothing, and 'cleaned' file
23
24 download) in approximately 30 minutes.
25
26
27
28
29
30

31 *Proof-of-concept: metals, inflammation and low birth weight*

32

33
34 Low birth weight (LBW; birth weight < 2500 g, regardless of gestational age)
35
36 is a significant predictor of infant morbidity and mortality.^{13,14} Inflammation in the
37
38 placenta is believed to be a major pathway of LBW in preterm pregnancies,¹⁵ but the
39
40 source of this inflammation is not always known. As a proof-of-concept to
41
42 demonstrate how our workflow could be used to explore the relationships between
43
44 trace metals and placental inflammation in LBW—and to demonstrate how elemental
45
46 imaging can be integrated with other imaging techniques—we stained for CD3, CD8,
47
48 CD68, and CD66b using 3-amino-9-ethylcarbazole (AEC)-based multiplexed
49
50 immunohistochemistry in a single tissue section sampled from the fetal side of the
51
52 placenta from a LBW birth (2,185 g; born at 35 weeks gestation) and normal weight
53
54 birth (2,828 g; born at 34 weeks gestation); both infants were male and delivered *via*
55
56
57
58
59
60

1
2
3 Cesarean section (**Figure 2**). Expression of inflammatory markers CD68 (marker of
4
5 macrophages) and CD66b (marker of neutrophils) was markedly increased in the
6
7 chorionic villi of the LBW placenta (**Fig. 2a**).
8
9

10 Visual inspection of the low-resolution stains for the LBW section identified
11
12 one site of CD66b accumulation (Site 1) and another site of CD68 accumulation (Site
13
14 2; **Fig. 2a**). In an adjacent section in the LBW placenta, we performed LA-ICP-MS
15
16 imaging (40- μm spot size; pixel area = 1600 μm^2) for Fe, Zn, Mn, Pb, and Cd (**Fig.**
17
18 **2b**). Although Cd was below detection limits, we found unique distributions for the
19
20 other elements that appeared to coincide with these inflammation sites: e.g., Mn and
21
22 CD66b seemed to be found together at Site 1, and Zn and CD68 appeared to coincide
23
24 at Site 2 (**Fig. 2b**).
25
26
27

28 To explore the relationships between the inflammatory markers and metals in
29
30 a more quantitative manner, we constructed a multilayered map in which the AEC
31
32 stain images and elemental maps were registered to the same spatial coordinate
33
34 system (**Fig. 2c**). We aligned the AEC stain images using automated 2D rigid body
35
36 image registration, then registered the element maps to the histologically stained
37
38 images by manually selecting tie points (corresponding features) between the stains
39
40 and the tissue mask layer using QGIS 2.10.1,¹⁶ an open-source geographic
41
42 information systems (GIS) program. We classified the AEC stains by separating the
43
44 hematoxylin and AEC stains using color deconvolution and applying an intensity
45
46 threshold algorithm to identify positive and negative pixels. Our final GIS map
47
48 structure consisted of the AEC base images with spatially-registered elemental maps
49
50 and AEC-positive areas for each cell surface marker that could be easily overlaid
51
52
53
54
55 (**Fig. 2c**).
56
57
58
59
60

1
2
3 Based on the image overlays at Site 2, CD68-positive areas appeared to
4 coincide with Zn hotspots (**Fig. 2d**). We identified element hotspots at Site 1 and Site
5 2 using site-specific Getis-Ord G_i^* analyses, which objectively identifies areas of
6 high and low element accumulation (details in **Materials and Methods**). We
7 quantified the overlap between the CD68-positive regions and element hotspots (Getis
8 Ord G_i^* z-scores > 1.96) using the ‘cell surface marker fractional’ (f_{CDx} : fraction of
9 cell surface marker-positive pixels that were also classified as element hotspots) and
10 confirmed that all CD68-positive pixels were also Zn hotspots ($f_{CD68} = 1.00$) at Site 2.
11 While the CD66b-positive regions at Site 1 appeared to possibly colocalize with
12 hotspots for both Mn and Zn, the f_{CD66b} scores for the Mn and Zn hotspots showed less
13 evidence of strong colocalization (Mn, $f_{CD66b} = 0.33$; Zn, $f_{CD66b} = 0.39$).
14
15
16
17
18
19
20
21
22
23
24
25
26
27
28
29
30
31
32
33
34
35
36
37
38
39
40
41
42
43
44
45
46
47
48
49
50
51
52
53
54
55
56
57
58
59
60

Discussion

The placenta is critical in maintaining the health of the fetus, and biomarkers of placenta-mediated changes to the intrauterine environment may serve as predictors of future health disorders.^{17,18} Recognizing the central role of the placenta in fetal development, major initiatives, including the Human Placenta Project of the US National Institutes of Health, have been instigated to develop novel methods for better understanding of how placental function is affected by a variety of external stressors.^{19,20} To uncover the role of environmental chemical exposures in fetal programming, it is important to characterize the pathways connecting environmental exposures, often occurring as complex mixtures of chemicals, with the biologic responses elicited within the placenta and to the effects on the developing fetal systems.¹⁸ Traditional approaches to analyzing placentae have not considered its complex architecture but have instead analyzed bulk chemical concentrations in tissue segments,²¹ which does not uncover regional variations in placental chemical processing that is likely cell-specific.

To overcome this barrier—and as a step toward the integration of MSI in human exposomic research—we developed a rapid and automated elemental image processing workflow for the quantitative assessment of the biologic impacts of complex metal mixtures. Our overarching goal was to develop an approach to consider the spatial distributions of metal exposures with cellular response proteins in human placental tissues. By doing so, we believe additional information on chemical effects can be deciphered when compared to standard methods that use whole tissues to measure chemical exposures or protein expression.

To demonstrate the potential of our method in health outcome research, we investigated the associations between metals and inflammatory markers in placental

1
2
3 sections from a LBW case and a typical birth weight control. We also display the
4
5 versatility of our workflow, which readily integrates multielemental MSI imaging
6
7 with data generated from other modalities (chromogen-based stains in this case).
8
9
10 Using quantitative spatial statistics, we observed that sites of inflammation coincided
11
12 with variations in Fe, Mn and Zn. While we intended for this sample to serve as a
13
14 proof-of-concept of our workflow and thus do not draw any biological conclusions
15
16 from the metal/protein associations, we note that previous reports have observed
17
18 complex relationships of Zn and Mn with neutrophil and macrophage activities.^{22,23}
19
20 Although no inferences can be drawn from the current study, we propose that the
21
22 integration of elemental imaging with immune marker detection has the potential to
23
24 provide insight into the roles of these metals in the immune response in future studies.
25
26 We used formalin-fixed, paraffin-embedded tissues to test the applicability of this
27
28 method for banked human samples. However, our workflow can be readily applied to
29
30 tissues prepared with other methods, such as frozen sections, when there are concerns
31
32 that fixation may perturb elemental signatures.²⁴⁻²⁶
33
34
35
36
37
38

39 **Conclusions**

40
41
42 Broadly, the workflow we present here can be used to quantitatively explore
43
44 the relationships between metal mixture exposures and biologic response mediators in
45
46 placenta and other tissues. The multiplexed nature of these assays make them
47
48 amenable to data-driven computational approaches to identify disease-relevant
49
50 interactions between metals and physiologic pathways, and are a crucial step towards
51
52 the application of MSI in uncovering the role of the placental exposome in fetal
53
54 programming of life-long health trajectories.
55
56
57
58
59
60

Materials and Methods

Sample collection and processing

Samples were collected from mother-child dyads enrolled from hospitals in Mexico City, Mexico. All subjects provided informed consent, and study protocols were approved by the Institutional Review Boards of all participating institutions. Placental tissues were sampled immediately after birth and placed in 4% neutral formaldehyde for transport. After arrival at the laboratory, the maternal, maternal decidua, and fetal zones were identified, and a small fragment from each zone was collected and fixed in 4% neutral formaldehyde overnight. The fragments were embedded in paraffin, cut to 5-um sections, and affixed to glass microscope slides, which were preserved at 4°C until use.

Cell surface marker immunohistochemistry

Placental sections were dewaxed in xylene and rehydrated in decreased concentrations of ethanol (EtOH) to pure water. Sections were incubated in Target Retrieval Solution pH 9.0 (Dako, S2367) for antigen retrieval (95°C, 30 minutes). Sections were incubated with 3% hydrogen peroxide and protein block serum-free (Dako, X0909) before adding primary antibody (CD3, clone 2GV6) followed by secondary antibody coupled with biotin. The binding of biotinylated antibodies was revealed by streptavidin-horseradish peroxidase, and peroxidase activity was revealed using 3-amino-9-ethylcarbazole (AEC, Vector, SK-4200). Tissue sections were then counterstained with hematoxylin Harris modified (Sigma, HHS16) and the slides mounted with aqueous mounting medium. Images were acquired using an Olympus whole-slide scanner operated with Olyvia software. After scanning, the CD3 staining was bleached and the slides subjected to another cycle of tagging (MICSSS method,

1
2
3 Remark et al., submitted). Thus, the same slides were stained for CD8 (clone
4 C8/144b) using Target Retrieval Solution pH 9, for antigen retrieval, scanned and de-
5 stained. By following the same workflow, the same slides were then sequentially
6 stained for CD68 (clone KP1) and CD66b (clone G10F5) using 10 mM citrate buffer
7 pH 6 and Target Retrieval Solution pH 9 for antigen retrieval, respectively.
8
9

10 11 12 13 *LA-ICP-MS analysis*

14
15
16
17 A New Wave Research NWR-193 laser ablation system was connected to an
18 Agilent Technologies 8800 ICP-MS by Tygon® tubing. A flow of 0.8 L min⁻¹ He gas
19 carried ablated material from the ablation chamber and was mixed with 0.65 L min⁻¹
20 Ar via a y-piece prior to the ICP-MS. A 40 µm diameter laser beam was rastered at a
21 speed of 100 µm s⁻¹. ICP-MS isotope dwell times for manganese (⁵⁵Mn), iron (⁵⁶Fe),
22 zinc (⁶⁶Zn), cadmium (¹¹¹Cd) and lead (²⁰⁸Pb) were adjusted to maintain sample
23 dimensions²⁷ (data points that correspond to a pixel size of approximately 40 × 40
24 µm). Laser fluence and repetition rate was optimized for ablation of the tissue whilst
25 preventing ablation of the underlying glass slide (0.5 J cm⁻², 40 Hz). A 3.0 mL min⁻¹
26 flow of H₂ in the ICP-MS octopole reaction system (ORS®) was used to minimize
27 interferences and improve signal stability.²⁸ In the absence of suitable tissue
28 standards, the certified reference material NIST612 glass was used to correct signal
29 variation between analyses and provide indicative concentration values. LA-ICP-MS
30 quantification is dependent on sample matrix;²⁹ therefore, the concentration values
31 provided in this study are considered semi-quantitative.
32
33
34
35
36
37
38
39
40
41
42
43
44
45
46
47
48
49

50 51 *LA-ICP-MS data processing*

52
53
54 Following LA-ICP-MS imaging, ablation line-specific .csv files generated by
55 the MassHunter Workstation software (Agilent) were read into RStudio (version
56
57
58
59
60

0.98.1102),³⁰ and CPS values for each element were coerced into a list of m by n element-specific matrices, where m = number of ablation lines and n = number of ablation spots per ablation line. For each matrix, row-specific gas blank CPS medians—which here corresponded to the median values in pixels (ablation spots) collected during the first 10 s of each ablation line—were subtracted from each pixel in the corresponding row. Gas-blank corrected matrices were converted to the RasterStack format using the R package ‘raster’,¹¹ where each $X_{m \times n}$ matrix was converted to a RasterLayer with spatial extent ($x_{\min} = 0$, $x_{\max} = n$, $y_{\min} = 0$, $y_{\max} = m$).

Image segmentation and background removal

Image segmentation into target and background pixels is often achieved using histogram-based thresholding of grayscale images, such as Otsu’s method.³¹ Here, we designed a histogram-based global thresholding algorithm that could be applied to LA-ICP-MS multidimensional imaging data. In an elemental imaging stack, element CPS values follow a finite mixture distribution with two component distributions,

$$f(x) = w_{tissue}p_{tissue}(x) + w_{back}p_{back}(x),$$

where $p_{tissue}(x)$ and $p_{back}(x)$ represent the probability density functions for tissue and background pixels, respectively, and w = weights where $w_i \geq 0$ and $w_{tissue} + w_{back} = 1$. (1)

Additionally, there is a varying level of shot (background) noise, which follows a

Poisson distribution that can be approximated by a Gaussian distribution,

$$p_G(x) = \frac{1}{\sigma\sqrt{2\pi}} e^{-\frac{(x-\mu)^2}{2\sigma^2}}. \quad (2)$$

Our algorithm derives a global threshold cutoff value from a single composite image created from an element RasterStack, with a method designed to (i) identify and remove elements with high background noise and (ii) place more weight on elements with higher tissue to background signals (x_{tissue}/x_{back}). First, CPS values for each

1
2
3 element were scaled and centered to generate standardized scores (z -scores), and
4
5 elements with high background noise (high z -score variability in gas-blank regions
6
7 based on a user-defined cutoff; here, standard deviation (s) > 0.15) were removed
8
9 from the element stack. Next, a single composite layer (CL) was created by
10
11 calculating the mean z -score for each pixel among all remaining element layers in the
12
13 stack, with elements weighted by the squared z -score mean in pixels located in their
14
15 gas-blank region, such that

$$16 \quad CL_{ij} = \frac{\sum_{k=1}^n w_k (x_{ij})_k}{\sum_{k=1}^n w_k}, \quad (3)$$

17
18 where n = number of RasterLayers in the stack, $(x_{ij})_k$ = z -score for pixel (i,j) in
19
20 RasterLayer X_k , and w_k = squared z -score mean in the gas-blank region of X_k , since
21
22 elements with a better ability to differentiate between tissue and background will have
23
24 z -scores in gas-blank pixels that deviate further below the overall image z -score mean
25
26 of 0. From the vectorized values in this composite layer, the kernel density function
27
28 was estimated using the R function *density*. The basic kernel density estimator can be
29
30 expressed as follows,
31
32

$$33 \quad \hat{f}_{kde}(x) = \frac{1}{n} \sum_{i=1}^n K\left(\frac{x - x_i}{h}\right), \quad (4)$$

34
35 where K = kernel and h = bandwidth; here, our algorithm uses a Gaussian kernel and
36
37 the “nrd0” bandwidth selector, which defaults to Silverman’s “rule of thumb”,³²
38
39

$$40 \quad h = 0.9 \min\left\{\sigma, \frac{R}{1.34}\right\} n^{-1/5}, \quad (5)$$

41
42 where R = the interquartile range $X_{[0.75n]} - X_{[0.25n]}$. The cutoff value for background
43
44 masking (n_{cutoff}) was calculated by finding the first-occurring local minimum value
45
46 from the $n = 512$ equally-spaced points at which the density was estimated.
47
48
49
50
51
52
53
54
55
56
57
58
59
60

Background pixels (*BP*) were classified by thresholding the weighted mean *z*-scores in the composite mask layer based on the criterion

$$BP(i, j) = \begin{cases} 1 & \text{if } (i, j) < n_{\text{cutoff}} \\ 0 & \text{if } (i, j) \geq n_{\text{cutoff}}. \end{cases} \quad (6)$$

All corresponding *BP* pixels in the mask layer were set to null (NA), while values in non-*BP* pixels were not changed.

After background thresholding, remaining pixels in the background region were removed using an automated clump deletion algorithm. First, unique ‘clumps’, or patches of connected pixels, were detected and assigned unique IDs using the *clump* function in the ‘raster’ package, with cells considered adjacent based on the Rook’s case contiguity rule. Next, all unique clumps in the mask layer that were comprised of less than a user-defined number of pixels (here, all clumps of ≤ 3 pixels) were assigned null (NA) values. A small group of remaining background clumps in the LBW sample mask was removed by manually drawing a polygon around the region using a region-of-interest selection tool (the *drawPoly* function in the ‘raster’ package) and setting pixels within this polygon region to NA. In the final step of the creation of the mask layer, tissue edges were identified based on Rook’s case contiguity using the *boundary* function in the ‘raster’ package. Pixels in the final mask (FM) layer were represented by values

$$FM_{ij} = \begin{cases} 1 & \text{if } (i, j) = \text{tissue edge} \\ 0 & \text{if } (i, j) = \text{inner tissue} \\ \text{NA} & \text{if } (i, j) = \text{background}. \end{cases} \quad (7)$$

Masked element stacks were created by assigning NA values to all pixels identified as background (NA) pixels in the mask layer, uniformly across each layer in the stack.

Outlier identification and spatial smoothing

We designed a local outlier detection algorithm to identify and replace local extreme, right-tail outliers that were likely to result from random shot noise and/or other instrumentation-related issues. Since LA-ICP-MS is a scanning technique, adjacent pixels in the y -axis are not collected sequentially, but are instead separated by a time overhead as the laser is rastered across the sample in x -axis rows. Thus, outliers that cluster along both the x - and y -axes are less likely to be due to random instrumentation fluctuation and more likely to reflect true biological variance. First, outliers were identified in masked element grids using a moving-window (user-defined dimensions; here, 7×7 pixels) method, where the median absolute deviation (MAD),

$$MAD = \frac{1}{n} \sum_{k=1}^n |x_k - m(X)|, \quad (8)$$

was calculated for 7×7 moving windows using the *focal* function in the ‘raster’ package, and pixels with values deviating from the local median at a user-defined magnitude greater than the MAD (here, 5 times) were classified as outliers. Next, a cluster identification algorithm identified outliers that were present in clusters occurring in ≥ 2 rows, which were reclassified as non-outlier pixels. Remaining outliers were assigned null values and replaced using a user-defined filter (here, a 3×3 median filter), which only replaced values in tissue-associated (non-background) pixels with null values. Finally, all non-null pixels in the masked images were spatially smoothed using a Gaussian smoothing operator,

$$G(i, j) = \frac{1}{2\pi\sigma^2} e^{-\frac{i^2+j^2}{2\sigma^2}}, \quad (9)$$

where $\sigma = 2/3$; the default radius in the *focalWeight* function in the ‘raster’ package, which was used here for spatial smoothing, is 3σ . The masked and smoothed

1
2
3 elemental images were the final images used for all subsequent statistical analyses.
4
5 (Note: prior to spatial smoothing, the shinyImaging application replaces outliers using
6
7 a weighted mean 7 x 7 filter [Gaussian filter: $\sigma=1$, $r=3$] rather than a median filter).
8
9

10 *Integration of data from elemental imaging and immunohistochemistry*

11
12 Cell surface marker (AEC) images (.vsi files) were imported into ImageJ
13
14 1.49v and converted to RGB color images. The images were background subtracted,
15
16 compiled into a stack, and aligned using 2D rigid body image registration with the
17
18 StackReg plugin.³³ After unstacking the images, positive AEC pixels were identified
19
20 by separating the hematoxylin and AEC stains with the “H AEC” vector in the Color
21
22 Deconvolution 1.7 plugin, then applying a global threshold (using Tsai’s method³⁴) to
23
24 the 8-bit AEC-separated images. The registered original images and segmented AEC-
25
26 positive images were saved as .tif files, which were each imported into QGIS 2.10.1¹⁶
27
28 as raster layers within a project file. To register the element maps to the cell surface
29
30 marker images, the tissue mask (.asc file) was opened in the QGIS Georeferencer, tie
31
32 points (corresponding features) were manually selected between the tissue mask and
33
34 the stain images, and the mask was aligned to the stains using a thin plate spline
35
36 transformation. Tie point coordinates were saved and used to register the element .asc
37
38 files, which were saved as raster layers in the project file.
39
40
41
42
43

44 *Statistical analysis of analyte colocalization*

45
46 We used a Getis-Ord G_i^* hotspot analysis³⁵ for an objective method to
47
48 identify statistically-significant areas of high and low element accumulation. Here, the
49
50 Getis-Ord G_i^* statistic was calculated for each element raster using the *lisa* function
51
52 in the ‘usdm’ R package³⁶, using a local neighborhood size corresponding to 175 μm ,
53
54 and pixels with z -scores ≥ 1.96 or ≤ -1.96 were classified as significant ‘hotspots’ or
55
56
57
58
59
60

1
2
3 ‘coldspots,’ respectively. To assess the degree of overlap between element hotspots
4 and immune marker-positive regions (AEC-positive regions) using a method similar
5 to the Manders overlap coefficient³⁷, we calculated three scores originally proposed
6 by Nawaz *et al.*³⁸:
7
8
9
10

- 11 1. Cell surface marker fractional (f_{CDx}): fraction of AEC-positive regions that
12 were also element hotspots;
13
- 14 2. Element hotspot fractional ($f_{element}$): fraction of element hotspots that were also
15 AEC-positive regions; and
16
- 17 3. Overlap fractional ($f_{overlap}$): fraction of AEC-positive regions and/or element
18 hotspots that were both AEC-positive regions and element hotspots (different
19 from the colocalization statistic proposed by Nawaz *et al.*³⁵).
20
21
22
23
24
25
26
27
28
29
30

31 **Acknowledgements:** We thank Joseph Gilbert for his help with the collection and
32 preparation of the placental tissues. M.A. is supported by DP2ES025453 (New
33 Innovator Award) and R00ES019597 from the National Institutes of Health. R.O.W.
34 is supported by P30ES023515, R01ES013744, and R01ES021357 from the National
35 Institutes of Health.
36
37
38
39
40
41
42
43
44
45
46
47
48
49
50
51
52
53
54
55
56
57
58
59
60

References

1. Cui Y, Zhu YG, Zhai R, Huang Y, Qiu Y, Liang J. 2005. Exposure to metal mixtures and human health impacts in a contaminated area in Nanning, China. *Environment International* 31:784-790.
2. Hu H, Shine J, Wright RO. 2007. The challenge posed to children's health by mixtures of toxic waste: The Tar Creek Superfund site as a case-study. *Pediatric Clinics of North America* 54:155-175.
3. Robinson O, Vrijheid M. 2015. The pregnancy exposome. *Current Environmental Health Reports* 2:204-213.
4. De Felice A, Ricceri L, Venerosi A, Chiarotti F, Calamandrei G. 2015. Multifactorial origin of neurodevelopmental disorders: approaches to understanding complex etiologies. *Toxics* 3:89-129.
5. Wild CP. 2012. The exposome: From concept to utility. *International Journal of Epidemiology* 41:24-32.
6. McDonnell LA, Heeren RM. 2007. Imaging mass spectrometry. *Mass Spectrometry Reviews* 26:606-643.
7. Hare DJ, New EJ, de Jonge MD, McColl G. 2015. Imaging metals in biology: Balancing sensitivity, selectivity and spatial resolution. *Chemical Society Reviews* 44:5941-58.
8. Pozebon D, Scheffler GL, Dressler VL, Nunes MAG. 2014. Review of the applications of laser ablation inductively coupled plasma mass spectrometry (LA-ICP-MS) to the analysis of biological samples. *Journal of Analytical Atomic Spectrometry* 29:2204-2228.
9. Austin C, Niedzwiecki M, Arora M. 2016. Multielemental bioimaging of tissues in children's environmental health research. *Current Opinion in Pediatrics*, in press.
10. Hare DJ, Lei P, Ayton S, Roberts BR, Grimm R, George JL, et al. 2014. An iron-dopamine index predicts risk of parkinsonian neurodegeneration in the substantia nigra pars compacta. *Chemical Science* 5:2160.
11. Hijmans RJ. 2015. Raster: Geographic data analysis and modeling. R package version 2.3-24.
12. Chen TW, Lin BJ, Brunner E, Schild D. 2006. In situ background estimation in quantitative fluorescence imaging. *Biophysical Journal* 90(7):2534-4.
13. McIntire DD, Bloom SL, Casey BM, Leveno KJ. 1999. Birth weight in relation to morbidity and mortality among newborn infants. *New England Journal of Medicine* 340:1234-1238.
14. McCormick MC. 1985. The contribution of low birth weight to infant mortality and childhood morbidity. *The New England Journal of Medicine* 312:82-90.

15. Mwanyumba F, Inion I, Gaillard P, Mandaliya K, Praet M, Temmerman M. 2003. Placental inflammation and perinatal outcome. *European Journal of Obstetrics, Gynecology, and Reproductive Biology* 108:164-170.
16. QGIS Team. 2015. QGIS geographic information system. Open Source Geospatial Foundation Project.
17. Mairesse J, Lesage J, Breton C, Bréant B, Hahn T, Darnaudéry M, et al. 2007. Maternal stress alters endocrine function of the fetoplacental unit in rats. *American Journal of Physiology Endocrinology and Metabolism* 292:E1526-33.
18. Prouillac C, Lecoœur S. 2010. The role of the placenta in fetal exposure to xenobiotics: Importance of membrane transporters and human models for transfer studies. *Drug Metabolism and Disposition* 38:1623-1635.
19. Guttmacher AE, Maddox YT, Spong CY. 2014. The human placenta project: Placental structure, development, and function in real time. *Placenta* 35:303-304.
20. Kaiser J. 2014. Gearing up for a closer look at the human placenta. *Science* 344:1073.
21. Esteban-Vasallo MD, Aragonés N, Pollán M, López-Abente G, Pérez-Gómez B. 2012. Mercury, cadmium, and lead levels in human placenta: A systematic review. *Environmental Health Perspectives* 120:1369-1377.
22. Kehl-Fie TE, Skaar EP. 2010. Nutritional immunity beyond iron: a role for manganese and zinc. *Current Opinion in Chemical Biology* 14:218-224.
23. Ibs K-H, Rink L. 2003. Zinc-altered immune function. *The Journal of Nutrition* 133:1452S-1456S.
24. Hackett MJ, McQuillan JA, El-Assaad F, Aitken JB, Levina A, Cohen DD, et al. 2011. Chemical alterations to murine brain tissue induced by formalin fixation: Implications for biospectroscopic imaging and mapping studies of disease pathogenesis. *The Analyst* 136:2941-2952.
25. Sarafanov AG, Todorov TI, Kajdacsy-Balla A, Gray MA, Macias V, Centeno JA. 2008. Analysis of iron, zinc, selenium and cadmium in paraffin-embedded prostate tissue specimens using inductively coupled plasma mass-spectrometry. *Journal of Trace Elements in Medicine and Biology: Organ of the Society for Minerals and Trace Elements (GMS)* 22:305-314.
26. Punshon T, Chen S, Finney L, Howard L, Jackson BP, Karagas MR, Ornvold K. 2015. High-resolution elemental mapping of human placental chorionic villi using synchrotron X-ray fluorescence spectroscopy. *Analytical and Bioanalytical Chemistry* 407(22):6839-50.
27. Lear J, Hare D, Adlard P, Finkelstein D, Doble P. 2012a. Improving acquisition times of elemental bio-imaging for quadrupole-based LA-ICP-MS. *Journal of Analytical Atomic Spectrometry* 27:159-164.

- 1
- 2
- 3 28. Lear J, Hare DJ, Fryer F, Adlard PA, Finkelstein DI, Doble PA. 2012b. High-
- 4 resolution elemental bioimaging of Ca, Mn, Fe, Co, Cu, and Zn employing LA-
- 5 ICP-MS and hydrogen reaction gas. *Analytical Chemistry* 84:6707-6714.
- 6
- 7 29. Craig C-A, Jarvis KE, Clarke LJ. 2000. An assessment of calibration strategies for
- 8 the quantitative and semi-quantitative analysis of calcium carbonate matrices by
- 9 laser ablation-inductively coupled plasma-mass spectrometry (LA-ICP-MS).
- 10 *Journal of Analytical Atomic Spectrometry* 15:1001-1008.
- 11
- 12 30. R Team. 2015. Rstudio: Integrated development for R. Boston, MA:RStudio, Inc.
- 13
- 14 31. Otsu N. 1979. A threshold selection method from gray-level histograms. *IEEE*
- 15 *Transactions on Systems, Man, and Cybernetics* 9:62-66.
- 16
- 17 32. Silverman BW. 1986. Density estimation for statistics and data analysis.
- 18 *Monographs on Statistics and Applied Probability*, London: Chapman and Hall.
- 19
- 20 33. Thevenaz P, Ruttimann UE, Unser M. 1998. A pyramid approach to subpixel
- 21 registration based on intensity. *IEEE Transactions on Image Processing* 7:27-41.
- 22
- 23 34. Tsai W-H. 1985. Moment-preserving thresholding: A new approach. *Computer*
- 24 *Vision, Graphics, and Image Processing* 29:377-393.
- 25
- 26 35. Getis A, Ord JK. 1992. The analysis of spatial association by use of distance
- 27 statistics. *Geographical Analysis* 24:189-206.
- 28
- 29 36. Naimi B. 2013. Usdm: Uncertainty analysis for species distribution models. R
- 30 package version 1.1-12.
- 31
- 32 37. Manders EMM, Verbeek FJ, Aten JA. 1993. Measurement of co-localization of
- 33 objects in dual-colour confocal images. *Journal of Microscopy* 169:375-382.
- 34
- 35 38. Nawaz S, Heindl A, Koelble K, Yuan Y. 2015. Beyond immune density: Critical
- 36 role of spatial heterogeneity in estrogen receptor-negative breast cancer. *Mod*
- 37 *Pathol* 28:766-777.
- 38
- 39
- 40
- 41
- 42
- 43
- 44
- 45
- 46
- 47
- 48
- 49
- 50
- 51
- 52
- 53
- 54
- 55
- 56
- 57
- 58
- 59
- 60

Figure Legends

Fig. 1. Overview of LA-ICP-MS imaging workflow. (a) Formalin-fixed, paraffin-embedded placental tissues, sampled from the fetal aspect, were sectioned (5- μ m thick) and affixed to glass slides. Spatial distribution of multiple elements was determined using LA-ICP-MS, and data was read into R as a grid stack for image processing. (b) Background pixels were masked using a global thresholding algorithm. A raw mask file was created by converting the elements in the grid stack to z -scores, removing elements from the stack with high background noise, and finding the mean pixel z -scores across all elements in the stack, weighted on the squared gas-blank z -score means for each element. A threshold cutoff value was determined from the first-occurring local minimum value from the kernel density estimate of the weighted mean grid, and pixels with values below the cutoff were set to null values. Then, the algorithm removed small clusters of remaining background pixels and identified tissue edges. (c) Extreme outliers were detected using a focal median absolute deviation algorithm that ignored outliers in biologically-relevant clusters, and these outliers were replaced using a 3x3 median filter. After outlier replacement, images were smoothed using a Gaussian filter ($\sigma = 2/3$, $r = 2$).

Fig. 2. Metals and inflammation in a low-birth-weight placenta. (a) Left: immunohistochemical stains for inflammatory cell surface markers (CD3, CD8, CD66b, and CD68) in placentas from normal-weight and low-birth-weight pregnancies (scale bar = 100 μ m). Right: low-resolution stains in low-birth-weight placenta for CD66b and CD68 (scale bar = 2 mm) with higher-resolution images from sites of CD66b- and CD68-positive staining (Site 1 and Site 2, respectively; scale bar

1
2
3 = 500 μm). **(b)** Element maps for Fe, Mn, Pb, and Zn from adjacent serial section in
4
5 low-birth-weight placenta. Scale bar = 1 mm. **(c)** Immunohistochemical stains and
6
7 element maps were overlaid by registering the tissue mask to the stain image, then
8
9 creating a multilayered map with stain images, stain-positive pixels, and element
10
11 maps registered to the same spatial coordinate system. **(d)** Overlay of CD66b- and
12
13 CD68-positive regions with Getis Ord G_i^* hotspot and coldspots for Fe, Mn, Pb, and
14
15 Zn.
16
17
18
19
20
21
22
23
24
25
26
27
28
29
30
31
32
33
34
35
36
37
38
39
40
41
42
43
44
45
46
47
48
49
50
51
52
53
54
55
56
57
58
59
60

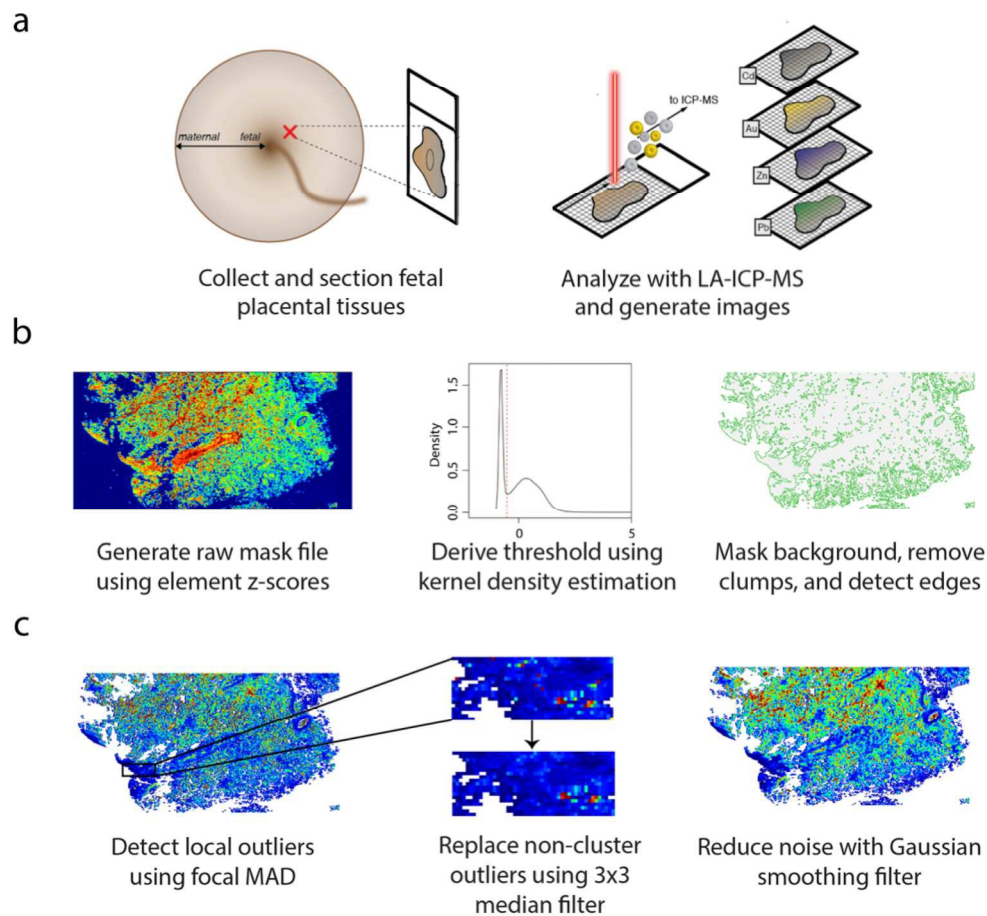


Fig. 1. Overview of LA-ICP-MS imaging workflow. (a) Formalin-fixed, paraffin-embedded placental tissues, sampled from the fetal aspect, were sectioned (5- μ m thick) and affixed to glass slides. Spatial distribution of multiple elements was determined using LA-ICP-MS, and data was read into R as a grid stack for image processing. (b) Background pixels were masked using a global thresholding algorithm. A raw mask file was created by converting the elements in the grid stack to z-scores, removing elements from the stack with high background noise, and finding the mean pixel z-scores across all elements in the stack, weighted on the squared gas-blank z-score means for each element. A threshold cutoff value was determined from the first-occurring local minimum value from the kernel density estimate of the weighted mean grid, and pixels with values below the cutoff were set to null values. Then, the algorithm removed small clusters of remaining background pixels and identified tissue edges. (c) Extreme outliers were detected using a focal median absolute deviation algorithm that ignored outliers in biologically-relevant clusters, and these outliers were replaced using a 3x3 median filter. After outlier replacement, images were smoothed using a Gaussian filter ($\sigma = 2/3$, $r = 2$). 201x190mm (300 x 300 DPI)

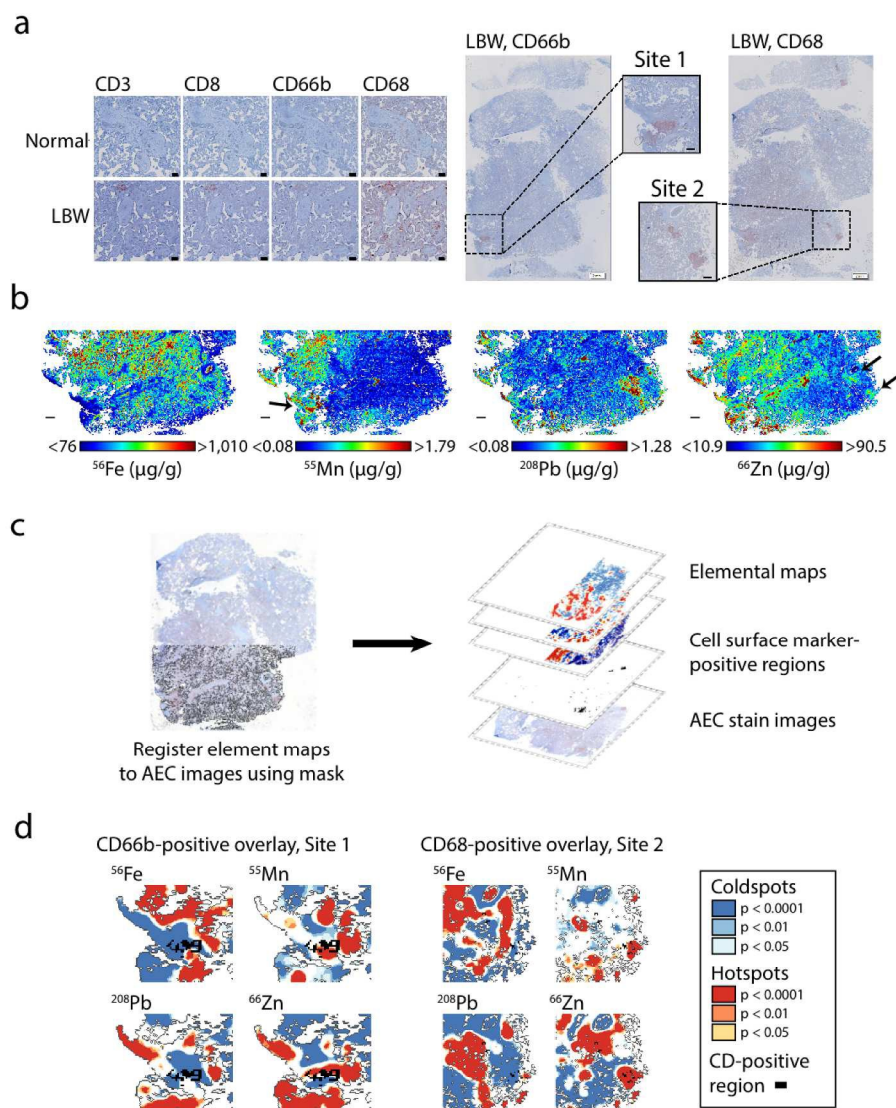


Fig. 2. Metals and inflammation in a low-birth-weight placenta. (a) Left: immunohistochemical stains for inflammatory cell surface markers (CD3, CD8, CD66b, and CD68) in placentas from normal-weight and low-birth-weight pregnancies (scale bar = 100 μm). Right: low-resolution stains in low-birth-weight placenta for CD66b and CD68 (scale bar = 2 mm) with higher-resolution images from sites of CD66b- and CD68-positive staining (Site 1 and Site 2, respectively; scale bar = 500 μm). (b) Element maps for Fe, Mn, Pb, and Zn from adjacent serial section in low-birth-weight placenta. Scale bar = 1 mm. (c) Immunohistochemical stains and element maps were overlaid by registering the tissue mask to the stain image, then creating a multilayered map with stain images, stain-positive pixels, and element maps registered to the same spatial coordinate system. (d) Overlay of CD66b- and CD68-positive regions with Getis Ord G_i^* hotspot and coldspots for Fe, Mn, Pb, and Zn. 186x241mm (300 x 300 DPI)